



Hydrous peridotitic fragments of Earth's mantle 660 km discontinuity sampled by a diamond

Tingting Gu^{1,2}, Martha G. Pamato³, Davide Novella³, Matteo Alvaro⁴, John Fournelle⁵, Frank E. Brenker⁶, Wuyi Wang¹ and Fabrizio Nestola^{3,6}

The internal structure and dynamics of Earth have been shaped by the 660 km boundary between the mantle transition zone and lower mantle. However, due to the paucity of natural samples from this depth, the nature of this boundary—its composition and volatile fluxes across it—remain debated. Here we analyse the mineral inclusions in a rare type IaB gem diamond from the Karowe mine (Botswana). We discovered recovered lower-mantle minerals ringwoodite + ferropericlasite + low-Ni enstatite (MgSiO₃) in a polyphase inclusion, together with other principal lower-mantle minerals and hydrous phases, place its origin at ~23.5 GPa and ~1,650 °C, corresponding to the depth at the 660 km discontinuity. The petrological character of the inclusions indicates that ringwoodite (~Mg_{1.84}Fe_{0.15}SiO₄) breaks down into bridgmanite (~Mg_{0.93}Fe_{0.07}SiO₃) and ferropericlasite (~Mg_{0.84}Fe_{0.16}O) in a water-saturated environment at the 660 km discontinuity and reveals that the peridotitic composition and hydrous conditions extend at least across the transition zone and into the lower mantle.

The 660 km discontinuity, demarcated by the abrupt changes in density and seismic wave velocities, is one of the global structures of our planet that controls heat and mass exchange between the surface and the deep interior. It is commonly accepted, on the basis of petrological evidence and laboratory observations, that the mantle transition zone (TZ), starting from ~410 km, is dominated by wadsleyite and ringwoodite, which have high water-storage capacities of 0.8–1.5 wt% H₂O^{1,2}. At ~660 km depth, ringwoodite, (Mg,Fe)₂SiO₄, the dominant TZ mineral between 520 and 660 km depth, disproportionates into bridgmanite (Mg,Fe)(Si,Al)O₃ and ferropericlasite (Mg,Fe)O³. The water-storage capacity of these lower-mantle (LM) minerals is much lower than that of wadsleyite or ringwoodite and shows a strong correlation with chemical compositions ranging from 100 ppm at ~25 GPa for pure Mg-bridgmanite^{4,5} to 2,000 ppm for Al- and Fe-bearing bridgmanite at similar conditions^{5,6}. The transportation of water beyond this region is critical to understanding of the global water cycle, as well as the compositional nature of the 660 km discontinuity.

However, it remains uncertain whether the chemical composition through the TZ–LM boundary is homogeneous or distinctly stratified^{7–9}. Geochemical analyses of the basaltic products of mantle melting in the upper mantle⁷ and elasticity measurements on Al-bearing bridgmanite at LM conditions⁹ suggest compositionally distinct upper and lower mantles. The compositional difference would not only affect partitioning of water and trace elements between the LM mineral assemblage¹⁰, but also play a role in the thermal stability of ringwoodite¹¹ and associated minerals¹². Recent small-scale seismic tomography data reveal rugged structures at the TZ–LM boundary¹³, suggesting regional chemical differences between the upper and lower mantles. Therefore, a partially restricted mantle circulation, alternating between layered and whole-mantle convection, raised questions about the compositional nature as well as the role that water plays at the 660 km discontinuity.

Direct samples from Earth's TZ and LM are rather scarce. Diamonds are one of the main sources that deliver samples from the most inaccessible regions to the surface. Inclusions enclosed by diamonds such as ice VII¹⁴, the hydrous phase EGG (AlSiO₃(OH))¹⁵ and ringwoodite with 1.5 wt% water¹⁶ indicate water saturation in the TZ around where diamonds form. However, it is unclear whether these samples represent a local water-saturated condition or an environment throughout the region. Although a few diamonds show ferropericlasite, enstatite (former bridgmanite) and olivine (former ringwoodite) as isolated inclusions or in composite pairs¹⁷ (Extended Data Fig. 1), these phases have never been reported all together as one single inclusion in assemblage, and whether these retrogressed mantle phases have a direct link with a hydrous environment was ambiguous.

Unearth a rare polyphasic mineral inclusion

In this Article, we report an intimate mineral assemblage found in a rare type IaB, 1.5 carat, D colour, polished gem diamond from the Karowe mine, Botswana (Methods and Extended Data Fig. 2). Within the diamond, except for a milky cluster (inclusion 3) composed of sub-micro-sized inclusions, a total of 12 composite and single-phase inclusions are visible (Supplementary Fig. 1), which were examined by micro-Raman spectroscopy and X-ray diffraction, including several that were exposed using a polishing wheel and Ar milling polisher at the surface for electron microprobe analysis (Supplementary Table 1).

Strikingly, among these inclusions, the diamond shows a mineral assemblage with ringwoodite in contact with ferropericlasite and enstatite (probably a polymorphic inversion from bridgmanite), which marks a scenario when ringwoodite began to break down into ferropericlasite and bridgmanite at the TZ–LM 660 km boundary. This assemblage, observed within inclusion 5 (Fig. 1), displays an opaque centre (~30 μm; Fig. 1) on the up-front side with an iridescent blue colour, which is often observed on ferropericlasite,

¹Gemological Institute of America, New York, NY, USA. ²The Department of Earth, Atmospheric, and Planetary Sciences, Purdue University, West Lafayette, IN, USA. ³Department of Geosciences, University of Padova, Padova, Italy. ⁴Department of Earth and Environmental Sciences, University of Pavia, Pavia, Italy. ⁵Department of Geoscience, University of Wisconsin, Madison, WI, USA. ⁶Department of Geoscience, Goethe University Frankfurt/TZ and LM arert, Frankfurt am Main, Germany. ✉ e-mail: gtt.pku@gmail.com; fabrizio.nestola@unipd.it

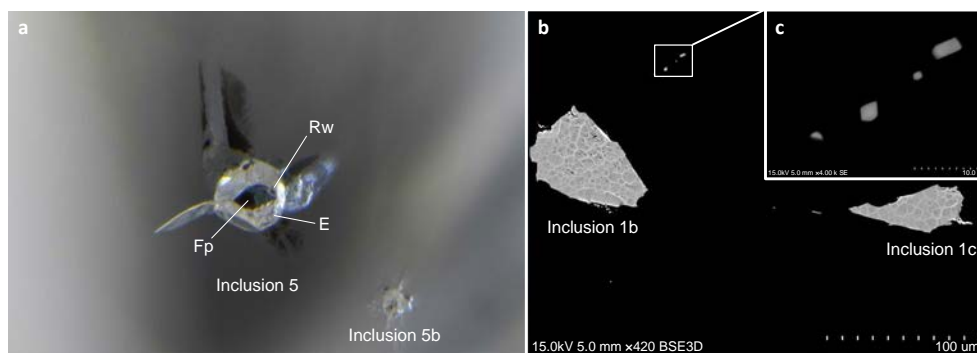


Fig. 1 | Photomicrographs of inclusions within a type IaB gem diamond from the Karowe mine, Botswana. **a**, Inclusion 5, imbedded in the diamond below the surface, containing the assemblage hydrous ringwoodite (Rw) + enstatite (En) + ferropericlasite (Fp). The smaller inclusion (Inclusion 5b) contains enstatite + olivine + magnesite (Supplementary Databases). Field view is 0.91 mm. **b**, Scanning electron microscope images of inclusions 1b and 1c, with the main grains containing enstatite. **c**, Enlarged image of exposed ringwoodite grains.

partially surrounded by a transparent inclusion portion of $\sim 80 \mu\text{m}$. At the boundary between the opaque and transparent portions of the inclusion, ringwoodite was identified by micro-Raman spectroscopy. The Raman bands at 803 and 839 cm^{-1} correspond to the asymmetric (T_{2g}) and symmetric (A_{1g}) stretching vibrations of SiO_4 tetrahedra in ringwoodite¹⁸ (Fig. 2a). Single-crystal X-ray diffraction, performed on the whole inclusion, identified ferropericlasite and enstatite (unit-cell parameters in Supplementary Table 2). X-ray diffraction spots assigned to ringwoodite are weak due to the very small crystal size (probably <10 microns). However, reflections at 2.02 \AA , 2.43 \AA and possibly 2.81 \AA are not overlapping with diamond, ferropericlasite or enstatite (Supplementary Fig. 2) and are confidently assigned to ringwoodite.

Moreover, in the same Raman spectrum that ringwoodite is detected, we also observe a strong band at $\sim 3,673 \text{ cm}^{-1}$ and a weaker but distinct band at $\sim 4,090 \text{ cm}^{-1}$ (Fig. 2b). The $4,090 \text{ cm}^{-1}$ peak is potentially due to the H–H stretching vibration in molecular H_2 dissolved in the lattice structure of ringwoodite, which has been observed in high-pressure experiments in olivine, orthopyroxene, clinopyroxene and garnet under reducing conditions¹⁹, and in omphacites from eclogites in Kaapvaal craton²⁰, but has not previously been reported in ringwoodite. The $3,673 \text{ cm}^{-1}$ band is consistent with OH stretching mode with H located at the edge of an octahedral silicate site²¹ or in a hydrous mineral phase such as brucite, serpentinite or talc with their OH stretching close to this region (Fig. 2b), which probably retrogressed from the hydrous mineral coexisting with ringwoodite or precipitate from the dehydration and breakdown of hydrous ringwoodite when the diamond was brought up to the surface. However, in the X-ray diffraction patterns, at least one diffraction peak consistent with brucite is observed in inclusion 5 (Supplementary Fig. 3). Therefore, a strained anisotropic brucite grain could possibly account for the origin of the OH peak at $\sim 3,673 \text{ cm}^{-1}$, with its peaks at the low-frequency region almost invisible due to their intensities being less than $\sim 20\%$ of that of OH stretching. Diamond anvil cell experiments²² simulating mantle downward flow demonstrated that brucite forms when hydrous ringwoodite is quenched to ambient condition under H_2O saturated conditions, which is similar to the scenario when the diamond is brought up to the surface transiently through explosive eruption. In our diamond, no growth zones or fractures extending to the surface have been observed under cathodoluminescence (Supplementary Fig. 5) around inclusion 5, which exclude the secondary or precursor origin of this inclusion. Although the ringwoodite grain in inclusion 5 is too small for Fourier-transform infrared spectroscopy (FTIR) study and the Raman signal of OH in ringwoodite at the Mg site from $\sim 3,000$ to $3,600 \text{ cm}^{-1}$ is not clear for a quantitative study

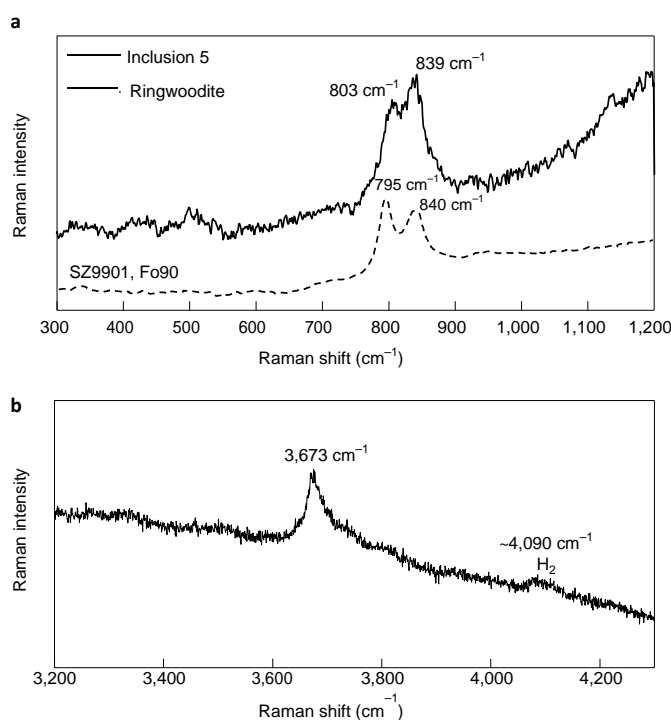


Fig. 2 | Raman spectra of inclusion 5. **a**, The low-wavenumber range, between 300 and $1,200 \text{ cm}^{-1}$. The spectra in solid lines represent ringwoodite in inclusion 5. For comparison, the spectra of synthetic hydrous Fo_{90} ringwoodite (run SZ9901 (ref. 18)) is shown in the dashed line. **b**, OH stretching and potentially molecular H_2 are observed in the high-wavenumber range. Source data

of H_2O content in this inclusion, the coexisting H vibration places the origin of the entrapped hydrous substance near the 660 km discontinuity.

other mantle slivers captured by this diamond

Beyond the polyphase inclusion 5, the 11 composite and single-phase inclusions in the diamond provide a more comprehensive petrological picture at this region. These inclusions were identified by Raman spectroscopy (Supplementary Databases and Extended Data Fig. 5) and X-ray diffraction (Supplementary Tables 1 and 2 and Supplementary Figs. 2–4) as enstatite, ringwoodite, ferropericlasite,

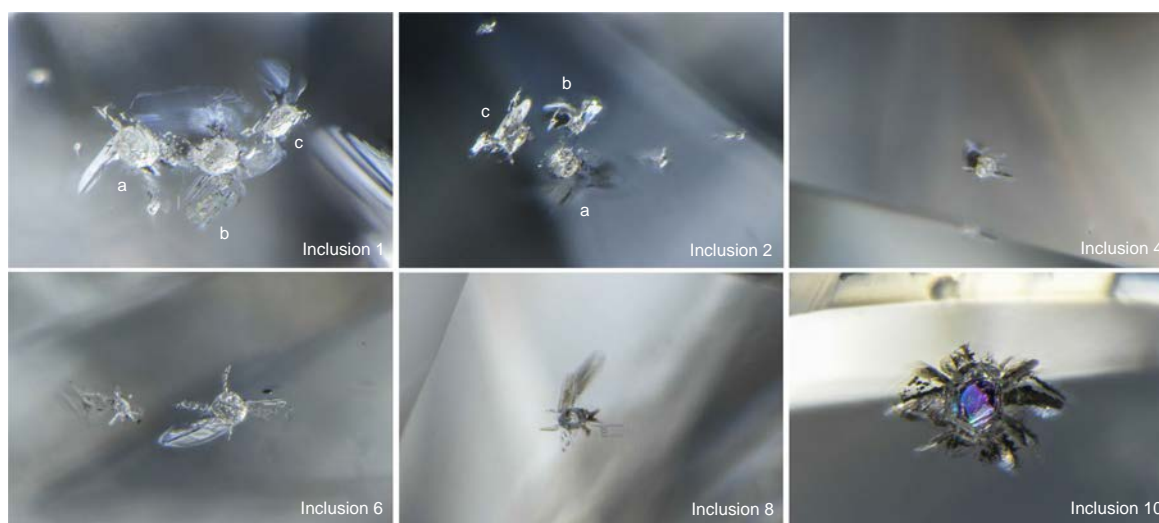


Fig. 3 | Photomicrographs of major inclusions in the 1.5 carat diamond investigated in this work, in addition to inclusions 5 and 11. Inclusions 1(a–c) and 2b, colourless and transparent, were identified as enstatite by micro-Raman spectroscopy (Supplementary Databases 1 and 3). Inclusion 1b also shows some minor portions of ringwoodite coexisting with enstatite (Supplementary Database 1). Inclusion 2a is a biphasic inclusion with enstatite in contact with a further grain of ringwoodite (showing the two typical peaks at approximately 806 and 840 cm^{-1} ; Supplementary Database 2). Raman spectroscopy performed on inclusion 2c showed bands corresponding to coesite and possibly phase D (Extended Data Fig. 5). In the same Raman spectrum, two peaks at 822 and 857 cm^{-1} are assigned to olivine as a back transformation from ringwoodite (Supplementary Database 4). Raman spectroscopy on inclusion 4 (Supplementary Database 5) indicates the presence of enstatite. However, an intense and broader band centred at $\sim 780\text{--}800\text{ cm}^{-1}$ could be attributed to a mineral with perovskite structure. Colourless and small ($<50\text{ }\mu\text{m}$) inclusion 6 was identified as enstatite (Supplementary Database 6). The small inclusion 8 (Supplementary Database 7) is identified as enstatite. Inclusion 10 is a large ($\sim 200\text{ }\mu\text{m}$) pseudo-hexagonal grain with a strong iridescence, which was identified by X-ray diffraction as ferropericlase. Note that bulk modules, component ratios and geometries of minerals will all affect the deformation and retrogression process of mineral inclusions in the diamond, and the high-pressure polymorph of the inclusions will not always be preserved. Field views of each image from inclusions 1, 2, 4, 6, 8 and 10 are 1.10, 0.96, 0.92, 1.20, 0.91 and 1.03 mm, respectively.

coesite (former stishovite) and perovskite-type mineral (Fig. 3 and Extended Data Figs. 3 and 4). Moreover, in inclusion 2c, coesite, which is probably derived from its high-pressure polymorph stishovite, is detected, accompanied by partially retrogressed ringwoodite, enstatite and ferropericlase (Supplementary Database 4). In addition, a few diffraction reflections, 4.13 and 4.30 Å (Supplementary Fig. 4), which do not overlap with coesite or ringwoodite/enstatite/ferropericlase (Supplementary Table 1), have been detected. Considering a few unassigned Raman peaks in the region of 300–1,000 cm^{-1} at ~ 787 , 735, 626 and 370 cm^{-1} , in addition to the band at 2,849 cm^{-1} (Extended Data Fig. 5), we could attempt an assignment of these features to phase D. Moreover, we found a diffraction peak at 2.99 Å that could be the most intense peak of Phase D ((101) reflection)²³. The occurrence of coesite has been observed from the breakdown of hydrous ringwoodite in a pyrolitic composition²⁴, and it was often observed accompanied by dense hydrous magnesium silicate (DHMS) phases in a hydrous ringwoodite system²⁵ or various compositions with $\text{MgO-SiO}_2\text{-Al}_2\text{O}_3\text{-FeO-H}_2\text{O}$ (ref. 12).

In addition to being in inclusion 5, ringwoodite was detected in inclusions 1b, 2a and 2c (Supplementary Databases 1 and 2). Importantly, four micrometre-sized grains (1–4 μm) were exposed during the final step of Ar milling and polishing near inclusion 1b (Fig. 1c). The two largest grains were analysed by electron microprobe analysis (EMPA), providing a composition of $\sim \text{Mg}_{1.84}\text{Fe}_{0.15}\text{SiO}_4$, consistent with that of ringwoodite (Supplementary Table 3). Two enstatite inclusions, 1b and 1c (Supplementary Table 4), were also exposed and show nearly identical chemical composition ($\text{Mg}_{0.928}\text{Fe}_{0.067}\text{Cr}_{0.004}\text{Mn}_{0.003}\text{Ti}_{0.003}\text{Na}_{0.002}(\text{Si}_{0.976}\text{Al}_{0.024})\text{O}_3$ (hereafter indicated as $(\text{Mg}_{0.93}\text{Fe}_{0.07})\text{SiO}_3$), which is consistent with the calculated composition of enstatite in inclusion 5 based on the equation of state and the unit-cell volume variation along the enstatite–ferrosilite binary join (Methods). These two enstatite crystals have NiO below

the detection limit, which is consistent with its high-pressure polymorph bridgmanite formed in equilibrium with ferropericlase, and a higher partition of Ni ($K_{\text{D-Ni}}$) in ferropericlase versus bridgmanite is expected with depth²⁶. The equilibrium is also readily reflected by the Ni content in ferropericlase of the exposed inclusion 11 (Extended Data Fig. 4), with chemical composition $(\text{Mg}_{0.840}\text{Fe}_{0.155}\text{Ni}_{0.012}\text{Na}_{0.003}\text{Cr}_{0.003}\text{Mn}_{0.001})\text{O}$ (hereafter indicated as $\text{Mg}_{0.84}\text{Fe}_{0.16}\text{O}$) (Supplementary Table 5). The Ni content is relatively high compared with that in ferropericlase enclosed by super-deep diamonds from other localities such as Juina, Kankan and Koffiefontein (Supplementary Fig. 1). The presence of multiple isolated ringwoodite, ferropericlase and enstatite grains in this diamond reinforced that the phase equilibrium observed in inclusion 5 is at the boundary of the 660 km discontinuity as the isolated ringwoodites can hardly reach equilibration at a lower pressure with the reaction of bridgmanite and ferropericlase.

The small sizes of the inclusions and their polyphase nature, as well as the potential loss of mineral sets when the diamond was faceted, restrict the ability to estimate mineral proportions and reconstruct the bulk composition of the protolith. However, the relatively abundant ferropericlase implies that the protolith of the inclusions captured by this diamond should have a relatively high Mg/Si ratio (>1). Moreover, the partition coefficient of Fe between bridgmanite and ferropericlase in this sample, which is calculated as 0.39 (Methods), shows a good match with that observed in a pyrolitic composition^{27,28}. On the basis of the thermodynamic expression describing the free energy change of the ion exchange reaction between bridgmanite and ferropericlase at equilibrium at $\sim 24\text{--}25\text{ GPa}$ (ref. 29) (Methods), we calculated the temperature corresponding to the Fe partition ratio, which is about 1,655 (± 200) °C, consistent with the geotherm at a depth of 660 km, and it provides a further constraint that enstatite would more likely be the

retrogressed phase of its high-temperature precursor bridgmanite instead of akimotoite (Extended Data Fig. 7). The relationship of Fe–Mg partitioning data and the Al content in bridgmanite also falls in the range of the results at ~24 GPa constrained by laboratory experiments (Extended Data Fig. 6)²⁹.

Hydrated nature of the 660 km discontinuity

The phase transition pressure of ringwoodite to bridgmanite has been constrained in previous laboratory experiments. Despite the broad range of discrepancies due to technical challenges, it has recently been reconciled by in situ experiments using a precise internal MgO pressure scale, and a transition pressure of ~23.51–24.07 GPa at ~1,472 °C for γ -Mg₂SiO₄ without Fe or Al was obtained³⁰. In a pyrolytic system, with the effects of incorporated cations such as Fe, Al and Ca, the transition pressure of ringwoodite was observed at ~23.5–24.5 GPa at ~1,600 °C, with a negative Clausius–Clapeyron slope^{24,31}. By contrast, the majorite–bridgmanite transition boundary has a positive Clapeyron slope²⁴; therefore, majorite is more stable at a higher temperature in a pyrolytic system. With a pure MgSiO₃ bulk composition, the majorite-to-bridgmanite transition can occur as low as ~21 GPa at ~1,600 °C (ref. ³²); however, the Al content has a strong effect on the majorite–bridgmanite transition pressure, which is ~23.5 GPa with ~3.6 wt% Al₂O₃ in the bulk pyrolytic system²⁴ and ~24.5 GPa with ~4.5 wt% bulk Al₂O₃ (ref. ³³), both at 1,600 °C (Extended Data Fig. 7). The mineral assemblages as well as the absence of majorite and the relatively low Al content in bridgmanite in our sample can match with a slightly depleted peridotitic composition at pressure ~23.7 GPa and temperature ~1,650 °C (Extended Data Fig. 7).

The petrological nature of the inclusions enclosed by this diamond therefore provides a coherent evidence of its origin from the 660 km discontinuity. The occurrence of ringwoodite together with the hydrous phases indicate a wet environment at this boundary. Although the formation of upper-mantle diamonds is often associated with the presence of fluids, super-deep diamonds with similar retrogressed mineral assemblages rarely have been observed accompanied with hydrous minerals¹⁷. The coexistence of hydrous minerals with enstatite, ferropiclasite and ringwoodite/olivine in this diamond further constrains the source of water is from the dehydration of ringwoodite; thus, a backward origin of ringwoodite from the reaction of bridgmanite and ferropiclasite in a much deeper realm would be less likely due to the low water-storage capacity of bridgmanite and ferropiclasite^{4–6}. The water-saturated condition is also reflected by the presence of magnesite near inclusion 5 (Supplementary Database 13), which could have been produced when the released water from ringwoodite interacted with carbonaceous material in deep Earth. However, the absence of the independent hydrous or carbonate minerals slims the possibility of the presence of an external aqueous fluid that is often associated with upper-mantle diamonds. The occurrence of hydrous phases such as brucite and DHMS phases with coesite balance the Mg/Si ratio in the system, rendering coesite a plausible phase in an ultramafic rock. The possible presence of phase D could potentially partition Al in the peridotitic system. Experimental studies revealed that Al shows a strong partitioning into DHMS phases with K_D around 10–15 at this depth³⁴, which means up to ~10% wt% Al₂O₃ could partition into phase D given that ~1.2 wt% Al was detected in enstatite (former bridgmanite). Incorporation of Al in DHMS phases substantially enhances their stabilities at high temperature, and the thermal stable temperature of phase D can reach 1,600 °C at 24 GPa in a MgO–SiO₂–Al₂O₃–H₂O system with only 1 wt% Al in the bulk composition¹². The occurrences of the hydrous minerals with the principal LM phases in a peridotitic mantle could potentially be the source of the seismic heterogeneity observed at the 660 km discontinuity¹³. Even though a local H₂O enrichment was suggested for the mantle

TZ based on the previous ringwoodite finding³⁵, the ringwoodite with hydrous phases, reported here—representative of a hydrous peridotitic environment at the TZ–LM boundary—indicates a more broadly hydrated transition zone down to and cross the 660 km discontinuity.

online content

Any methods, additional references, Nature Research reporting summaries, source data, extended data, supplementary information, acknowledgements, peer review information; details of author contributions and competing interests; and statements of data and code availability are available at <https://doi.org/10.1038/s41561-022-01024-y>.

Received: 24 January 2022; Accepted: 2 August 2022;

Published online: 26 September 2022

references

1. Fei, H. & Katsura, T. High water solubility of ringwoodite at mantle transition zone temperature. *Earth Planet. Sci. Lett.* **531**, 115987 (2020).
2. Fei, H. & Katsura, T. Water solubility in Fe-bearing wadsleyite at mantle transition zone temperatures. *Geophys. Res. Lett.* **48**, e2021GL092836 (2021).
3. Ito, E. & Takahashi, E. Postspinel transformations in the system Mg₂SiO₄–Fe₂SiO₄ and some geophysical implications. *J. Geophys. Res. Solid Earth* **94**, 10637–10646 (1989).
4. Bolfan-Casanova, N. Water in the Earth's mantle. *Mineral. Mag.* **69**, 229–258 (2005).
5. Litasov, K. et al. Water solubility in Mg-perovskites and water storage capacity in the lower mantle. *Earth Planet. Sci. Lett.* **211**, 189–203 (2003).
6. Murakami, M. Water in Earth's lower mantle. *Science* **295**, 1885–1887 (2002).
7. Allegre, C. J., Staudacher, T., Sarda, P. & Kurz, M. Constraints on evolution of Earth's mantle from rare gas systematics. *Nature* **303**, 762–766 (1983).
8. Hofmann, A. W. Mantle geochemistry: the message from oceanic volcanism. *Nature* **385**, 219–229 (1997).
9. Murakami, M., Ohishi, Y., Hirao, N. & Hirose, K. A perovskitic lower mantle inferred from high-pressure, high-temperature sound velocity data. *Nature* **485**, 90–94 (2012).
10. Liebske, C., Corgne, A., Frost, D. J., Rubie, D. C. & Wood, B. J. Compositional effects on element partitioning between Mg-silicate perovskite and silicate melts. *Contrib. Mineral. Petrol.* **149**, 113–128 (2005).
11. Ghosh, S. et al. Effect of water in depleted mantle on post-spinel transition and implication for 660 km seismic discontinuity. *Earth Planet. Sci. Lett.* **371–372**, 103–111 (2013).
12. Ghosh, S. & Schmidt, M. W. Melting of phase D in the lower mantle and implications for recycling and storage of H₂O in the deep mantle. *Geochim. Cosmochim. Acta* **145**, 72–88 (2014).
13. Wu, W., Ni, S. & Irving, J. C. E. Inferring Earth's discontinuous chemical layering from the 660-kilometer boundary topography. *Science* **363**, 736–740 (2019).
14. Tschauer, O. et al. Ice-VII inclusions in diamonds: evidence for aqueous fluid in Earth's deep mantle. *Science* **359**, 1136–1139 (2018).
15. Wirth, R., Vollmer, C., Brenker, F., Matsyuk, S. & Kaminsky, F. Inclusions of nanocrystalline hydrous aluminium silicate 'Phase Egg' in superdeep diamonds from Juina (Mato Grosso State, Brazil). *Earth Planet. Sci. Lett.* **259**, 384–399 (2007).
16. Pearson, D. G. et al. Hydrous mantle transition zone indicated by ringwoodite included within diamond. *Nature* **507**, 221–224 (2014).
17. Harte, B. Diamond formation in the deep mantle: the record of mineral inclusions and their distribution in relation to mantle dehydration zones. *Mineral. Mag.* **74**, 189–215 (2010).
18. Thomas, S.-M. et al. Quantification of water in hydrous ringwoodite. *Front. Earth Sci.* **2**, 38 (2015).
19. Yang, X., Keppler, H. & Li, Y. Molecular hydrogen in mantle minerals. *Geochem. Perspect. Lett.* **2**, 160–168 (2016).
20. Moine, B. N. et al. Molecular hydrogen in minerals as a clue to interpret δD variations in the mantle. *Nat. Commun.* **11**, 3604 (2020).
21. Keppler, H. Thermodynamics of water solubility and partitioning. *Rev. Mineral. Geochem.* **62**, 193–230 (2006).
22. Schmandt, B., Jacobsen, S. D., Becker, T. W., Liu, Z. & Dueker, K. G. Dehydration melting at the top of the lower mantle. *Science* **344**, 1265–1268 (2014).
23. Frost, D. J. & Fei, Y. Stability of phase D at high pressure and high temperature. *J. Geophys. Res. Solid Earth* **103**, 7463–7474 (1998).
24. Hirose, K. Phase transitions in pyrolytic mantle around 670-km depth: implications for upwelling of plumes from the lower mantle. *J. Geophys. Res.* **107**, 2078 (2002).

25. Chen, H. et al. Phase transformation of hydrous ringwoodite to the lower-mantle phases and the formation of dense hydrous silica. *Am. Mineral.* **105**, 1342–1348 (2020).
26. Stachel, T., Harris, J. W., Brey, G. P. & Joswig, W. Kankan diamonds (Guinea) II: lower mantle inclusion parageneses. *Contrib. Mineral. Petrol.* **140**, 16–27 (2000).
27. Wood, B. J. Phase transformations and partitioning relations in peridotite under lower mantle conditions. *Earth Planet. Sci. Lett.* **174**, 341–354 (2000).
28. Katsura, T. & Ito, E. Determination of Fe–Mg partitioning between perovskite and magnesiowüstite. *Geophys. Res. Lett.* **23**, 2005–2008 (1996).
29. Frost, D. J. & Langenhorst, F. The effect of Al₂O₃ on Fe–Mg partitioning between magnesiowüstite and magnesium silicate perovskite. *Earth Planet. Sci. Lett.* **199**, 227–241 (2002).
30. Ishii, T. et al. Complete agreement of the post-spinel transition with the 660-km seismic discontinuity. *Sci. Rep.* **8**, 6358 (2018).
31. Irifune, T. Absence of an aluminous phase in the upper part of the Earth's lower mantle. *Nature* **370**, 131–133 (1994).
32. Hirose, K., Komabayashi, T., Murakami, M. & Funakoshi, K.-I. In situ measurements of the majorite–akimotoite–perovskite phase transition boundaries in MgSiO₃. *Geophys. Res. Lett.* **28**, 4351–4354 (2001).
33. Ishii, T., Kojitani, H. & Akaogi, M. Phase relations and mineral chemistry in pyrolitic mantle at 1600–2200 °C under pressures up to the uppermost lower mantle: phase transitions around the 660-km discontinuity and dynamics of upwelling hot plumes. *Phys. Earth Planet. Inter.* **274**, 127–137 (2018).
34. Xu, C. et al. Al partitioning between phase D and bridgmanite at the uppermost lower mantle pressure. *Phys. Chem. Miner.* **48**, 37 (2021).
35. Keppeler, H. Earth's deep water reservoir. *Nature* **507**, 174–175 (2014).

Publisher's note Springer Nature remains neutral with regard to jurisdictional claims in published maps and institutional affiliations.

Springer Nature or its licensor holds exclusive rights to this article under a publishing agreement with the author(s) or other rightsholder(s); author self-archiving of the accepted manuscript version of this article is solely governed by the terms of such publishing agreement and applicable law.

© The Author(s), under exclusive licence to Springer Nature Limited 2022

Methods

FTIR spectroscopy. FTIR spectroscopy was conducted at Gemological Institute of America's New York lab using a Thermo Nicolet iS50 spectrometer equipped with XT-KBr beam splitters and an MCT-A detector. Absorption spectra were collected covering the 11,700–600 cm⁻¹ range. Background spectra of 32 scans were recorded before the analytical session. Spectra were collected with a resolution of 1 cm⁻¹. Instrument and sample chambers were purged with dried air to minimize absorption features from atmospheric water. Spectra were normalized on the basis of the height of the two-phonon absorption in diamond. The infrared active nitrogen concentration of this diamond (Supplementary Fig. 2), calculated from absorption coefficients at 1,282 cm⁻¹ (ref. 36), is approximately 66 ppm. The aggregation of B centre nitrogen is 100% as the A centre nitrogen (two neighbouring nitrogen atoms) was not detected. Pure type IaB diamonds are often associated with diamond suites of super-deep origin³⁷.

Single-crystal X-ray diffraction. X-ray diffraction measurements were performed using a Rigaku–Oxford Diffraction Supernova single-crystal diffractometer installed at the Department of Geosciences at the University of Padova. The instrument is equipped with a micro-X-ray source, MoK α , operating at 50 kV and 0.8 mA and with a Pilatus 200K Dectris detector³⁸. The beam size was 120 μ m during the analyses, and the sample-to-detector distance was 68 mm. Data collections were done on inclusions using a 0–360° rotation along the phi axis with exposure times between 10 and 300 seconds depending on the size of the inclusions. Data collected on inclusions suitable for X-ray diffraction measurements are reported in Supplementary Table 2.

Micro-Raman spectroscopy. Micro-Raman microscopy was performed on a Renishaw Invia Raman Microscope at the Gemological Institute of America. Laser output power was set to 17 mW and an 1,800 lines mm⁻¹ grating was used. A He–Ne laser was used, with a wavelength of 632.8 nm. The choice of laser was in part to avoid the luminescence peak from the diamond defect with zero-phonon line at 536 nm corresponding to a Raman shift at ~800 cm⁻¹ that occurs when a 514.5 nm laser is used. Lenses with magnification of $\times 50$ and $\times 20$ and 0.55 numerical aperture were used. Raman shift was calibrated by a silicon standard with its diagnostic peak at 520.5 cm⁻¹.

Raman spectra collected at Northwestern University were obtained using a custom-built, confocal optical path with Olympus-BX microscope, Melles Griot 458 nm solid-state laser, Andor Shamrock 0.3-m-focal-length spectrograph with 1,200 lines mm⁻¹ grating, Andor Newton DU970 CCD camera, $\times 100$ objective and 3–6 mW of laser power at the focal spot.

Microprobe analyses on inclusion 1 and inclusion 11. Enstatite inclusions were exposed by micro-diamond-embedded polishing disk at Gemological Institute of America. The whole diamond was mounted in epoxy for ion milling and analyses. The ferropericlasite and enstatite inclusions were initially 30–40 μ m below the surface of the host diamond with a non-flat surface apparently bearing debris from routine gem polishing. They were thinned using a Hitachi Ion Mill Polisher IM4000Plus, resulting in a smooth surface, with less than 0.5–1.0 μ m difference in surface depth relative to host diamond. Ferropericlasite and its standards as well as enstatite inclusions were Ir coated with a thickness of 1 nm with a Leica ACE600 high vacuum-sputter coater. The standards for enstatite had been previously coated with 20 nm of carbon.

EMPAs were performed at the Department of Geoscience, University of Wisconsin–Madison, using either a CAMECA SX51 or a CAMECA SXFiveFE electron probe, operating at 15 kV or 6 kV, and a 20 nA Faraday beam current with a fixed tight beam. For ferropericlasite Mg K α and O K α measurements were performed with the SX51 at 6 kV to minimize the matrix correction (mainly to reduce the absorption correction, from 60–70% to ~10%), and an oxygen jet (pressure 1×10^{-3} Pa) with LN-chilled cold plate were used to minimize hydrocarbon contamination. All the other elements were measured at 15 kV. The enstatite and the ringwoodite were analysed with the SXFiveFE. For enstatite, 15 kV with 20 nA Faraday beam current was used. For ringwoodite, both 15 kV and 10 kV with 20 nA Faraday beam current were used. The issue of low overvoltage for the Fe K α line results in a much larger analytical error for Fe (and not for Mg and Si), which was calculated as $\pm 15\%$. Counting time per point was 10 seconds on the peak and 10 seconds on the combined background points.

For wavelength-dispersive spectroscopy of ferropericlasite, the following analyser crystals were used: PCO (45 Å) for O K α ; TAP for Na, Mg, Al and Si K α ; PET for K, Ca, Ti, Cr and Mn K α ; and LiF for Fe and Ni K α . The PAP matrix correction and MAC30 mass absorption coefficients were used in the data treatment. Standards used were MgO, Fe_{0.92}O, Cr₂O₃, NiO, MnSiO₃ and albite (Na, Al, Si). Detection limits (wt%) for the low-abundance elements are as follows: Cr (0.007), Ni (0.013), Mn (0.018), Na (0.0140), Al (0.006) and Si (0.006). Grids of

points were set up and automated on the ferropericlasite and enstatite, with ~6 μ m spacing. We attempted to measure other elements in ferropericlasite (Ca, K and Ti) but they were below detection.

For wavelength-dispersive spectroscopy of enstatite, the following analyser crystals were used: LTAP for Na and Mg; TAP for Al and Si K α ; LPET for Ca and

Ti K α ; LiF for Fe and Mn K α ; and LLiF for V, Cr and Ni K α . The Armstrong–Scott Love matrix correction and associated mass absorption coefficients were used in the data treatment. Standards used were jadeite for Na and Al, synthetic enstatite for Mg and Si, augite for Ca, haematite for Fe, TiO₂ for Ti, tephroite for Mn, Cr₂O₃ for Cr, and V and Ni metals for those elements. Detection limits (element wt%) for the low-abundance elements are as follows: Na (0.01), Al (0.01), Ca (0.01), Ti (0.01), Mn (0.02), V (0.02), Cr (0.02), Ni (0.02), Mn (0.018); V and Ni were below detection.

For wavelength-dispersive spectroscopy of ringwoodite, the following analyser crystals were used: LTAP for Mg, TAP for Si K α , LPET for Ca K α , LiF for Fe and Mn K α , and LLiF for Cr and Ni K α . The Armstrong–Scott Love matrix correction and associated mass absorption coefficients were used in the data treatment. Standards used were synthetic forsterite for Mg and Si, augite for Ca, haematite for Fe, tephroite for Mn, Cr₂O₃ for Cr, and Ni metal for Ni. Detection limits (element wt%) for the low-abundance elements are as follows: Ca (0.01), Mn (0.06), Cr (0.04) and Ni (0.06); Ca, Cr and Ni were below detection.

Calculation of the residual pressure P_{inc} for ferropericlasite and the composition of enstatite in inclusion 5. Ferropericlasite is stable at most pressure and temperature conditions in the mantle and, therefore, when observed as an isolated mineral inclusion is not considered an unambiguous indicator of a super-deep origin³⁹. The presence of ringwoodite in the phase assemblage, however, confirms the super-deep origin of the diamond. The pressure exerted by the diamond host on the inclusion when the diamond is at room pressure is generally referred to as the residual pressure, P_{inc} . Here we can calculate the P_{inc} of ferropericlasite in inclusion 5 as in ref. 40, assuming the same composition of inclusion 11 (a homogeneity often observed within super-deep diamonds^{40,41}). To calculate P_{inc} , we used EoSFIT7-GUI software⁴² and the elastic properties for the ferropericlasite inclusions obtained by fitting the original pressure–volume–temperature (P – V – T) data⁴³ up to 2,000 K and 50 GPa. Using a third-order Birch–Murnaghan equation of state combined with a Berman-type thermal expansion, we obtained an isothermal bulk modulus $K_{0T} = 162(14)$ GPa.

Using the chemistry of ferropericlasite of inclusion 11, a unit-cell volume at room pressure equal to 75.80 Å³ (based on equation $X_{Fe} = 8.441 \times a(\text{Å}) - 35.553$, valid for stoichiometric ferropericlasite–magnesiowüstite at room pressure⁴⁴) was obtained. As the volume of ferropericlasite of inclusion 5 is 75.20 Å³ (Supplementary Table 2), we can estimate that the difference in volume is 0.60 Å³. Using the preceding bulk modulus, a $P_{inc} = 1.31$ GPa can be determined for inclusion 5.

Enstatite in inclusion 5 has a unit-cell volume $V = 825.1 \text{ Å}^3$ (Supplementary Table 2). Assuming the $P_{inc} = 1.31$ GPa determined on ferropericlasite (which is in contact with this enstatite) and using a bulk modulus $K_{0T} = 105.8(5)$ GPa and its first pressure derivative $K' = 8.5(3)$ for enstatite⁴⁵, we can calculate that the enstatite inclusion should have, at atmospheric pressure, a volume $V = 834.9 \text{ Å}^3$. This volume is consistent with an enstatite having an approximate composition equal to Mg_{0.93}Fe_{0.07}SiO₃. This composition is obtained using the unit-cell volumes for different compositions between pure MgSiO₃ and Mg_{0.56}Fe_{0.44}SiO₃ from the literature^{46–51} (which gives the following linear relationship: $V(\text{Å}^3) = -0.4502 \times \text{En}$ (mole fraction $\times 100$) + 876.73 and $V = 834.9 \text{ Å}^3$). Note that this calculation does not consider the possible presence of Al in the former bridgmanite, which, however, should be small (0.02 pfu)^{27,52}.

Calculation of the Fe partition coefficient between bridgmanite and ferropericlasite. The Fe partition coefficient between bridgmanite and ferropericlasite can be defined as

$$K_{Fe-Mg} = \frac{X_{Fe}^{Bm} / X_{Mg}^{Bm}}{X_{Fe}^{Fp} / X_{Mg}^{Fp}} \quad (1)$$

where X is the mol fraction of the element in the corresponding phase. Based on the EMPA data, the Fe partition coefficient calculated here is 0.39. The Mg–Fe partitioning equilibrium between bridgmanite and ferropericlasite in an Al₂O₃–free system is expressed as the following exchange reaction:



At the equilibrium, we have:

$$\mu_{\text{FeSiO}_3}^{\text{Bm}} + \mu_{\text{MgO}}^{\text{Fp}} = \mu_{\text{MgSiO}_3}^{\text{Bm}} + \mu_{\text{FeO}}^{\text{Fp}} \quad (3)$$

Where μ_i^X is a partial molar free energy of i component in phase X . The μ_i is expressed as

$$\mu_i^X = \mu_i^{\circ} + RT \ln a_i \quad (4)$$

where μ_i° is molar free energy of pure i component with the structure of phase X ; a_i^X is activity of i component in phase X , which can be expressed as:

$$a_i^X = (X_i^X \gamma_i^X) \quad (5)$$

where X_i^X and γ_i^X are mole fraction and activity coefficient, respectively.

Assuming that all components are the pure phase at the target pressure and temperature, then the standard free energy difference of equation (2) can be expressed as:

$$\Delta G^0 = -RT \ln \left[\frac{(a_{\text{FeSiO}_3}^{\text{Bm}} a_{\text{MgO}}^{\text{Fp}})}{(a_{\text{MgSiO}_3}^{\text{Bm}} a_{\text{FeO}}^{\text{Fp}})} \right] \quad (6)$$

By adopting a symmetric regular solution model for both bridgmanite and ferropericline solid solutions, the activity coefficient can be expressed as:

$$RT \ln \gamma_i^X = (1 - X_i^X) W_G^X \quad (7)$$

where W_G^X is the interaction parameter of phase X for one cation site basis.

By combining equations (3)–(7), the partition coefficient $K_{\text{Fe-Mg}}$ can be expressed in terms of interaction parameters and mole fractions as:

$$RT \ln K_{\text{Fe-Mg}} = \Delta G^0 + W_{\text{Fe-Mg}}^{\text{Bm}} (2X_{\text{Fe}}^{\text{Bm}} - 1) + W_{\text{Fe-Mg}}^{\text{Fp}} (1 - 2X_{\text{Fe}}^{\text{Fp}}) \quad (8)$$

We selected previous data from Fe–Mg partition experiments done with pure (Mg,Fe)SiO₃ and (Mg,Fe)O in a temperature range below 1,900 °C and pressure at ~24–25 GPa (refs. 28,29,53). The data were fitted by least-square fitting,

and the obtained parameters are $\Delta G^0 = 27,400 (\pm 540) \text{ J mol}^{-1}$; $W_{\text{Fe-Mg}}^{\text{Bm}} = 1, 200 (\pm 150) \text{ J mol}^{-1}$; $W_{\text{Fe-Mg}}^{\text{Fp}} = 17, 900 (\pm 840) \text{ J mol}^{-1}$; with $R^2 = 0.957$. All Fe are treated as Fe²⁺ on the basis of the EMPA data of enstatite with a total close to 100%, implying that the content of Fe³⁺ could be minor.

To consider the effect of Al, at fixed values of $X_{\text{Fe}}^{\text{Fp}}$, the Al O₃-bearing bridgmanite Fe/(Fe + Mg) ratio $X_{\text{Fe}}^{\text{Al,Bm}}$ as a function of Al content in MgSiO₃ formula unit can be expressed as:

$$X_{\text{Fe}}^{\text{Al,Bm}} = X_{\text{Fe}}^{\text{Bm}} + a X_{\text{Al}} \quad (9)$$

The coefficient a was adopted from a previous study²⁹ by a weighted least-squares regression fit to both Al₂O₃-free and Al₂O₃-bearing data, which gave $a = 3.67$. Our data match well with the range of Al content (~0.024 per formula unit) when Fe reaches equilibrium in bridgmanite and ferropericline at ~24 GPa according to previous experimental observation (Extended Data Fig. 6), and the calculated temperature at the phase equilibrium is 1,655 (±200) °C.

Data availability

All data are available in the main text or the supplementary materials; XRD raw data are available at <https://doi.org/10.6084/m9.figshare.20044727>. Source data are provided with this paper.

references

- Boyd, S. R., Kiflawi, I. & Woods, G. S. Infrared absorption by the B nitrogen aggregate in diamond. *Phil. Mag. B* **72**, 351–361 (1995).
- Motsamai, T., Harris, J. W., Stachel, T., Pearson, D. G. & Armstrong, J. Mineral inclusions in diamonds from Karowe Mine, Botswana: super-deep sources for super-sized diamonds? *Mineral. Petrol.* **112**, 169–180 (2018).
- Nestola, F. et al. Tetragonal almandine–pyrope phase, TAPP: finally a name for it, the new mineral jeffbenite. *Mineral. Mag.* **80**, 1219–1232 (2016).
- Brey, G. P., Bulatov, V., Gimis, A., Harris, J. W. & Stachel, T. Ferropericline—lower mantle phase in the upper mantle. *Lithos* **77**, 655–663 (2004).
- Anzolini, C. et al. Depth of diamond formation obtained from single pericline inclusions. *Geology* **47**, 219–222 (2019).
- Seitz, H.-M. et al. Ferropericline inclusions in ultradeep diamonds from Sao Luiz (Brazil): high Li abundances and diverse Li-isotope and trace element compositions suggest an origin from a subduction mélange. *Mineral. Petrol.* **112**, 291–300 (2018).
- Gonzalez-Platas, J., Alvaro, M., Nestola, F. & Angel, R. EosFit7-GUI: a new graphical user interface for equation of state calculations, analyses and teaching. *J. Appl. Crystallogr.* **49**, 1377–1382 (2016).
- Mao, Z., Lin, J.-F., Liu, J. & Prakapenka, V. B. Thermal equation of state of lower-mantle ferropericline across the spin crossover. *Geophys. Res. Lett.* **38**, L23308 (2011).
- Nimis, P. et al. Fe-rich ferropericline and magnesiowüstite inclusions reflecting diamond formation rather than ambient mantle. *Geology* **47**, 27–30 (2018).
- Angel, R. J. & Jackson, J. M. Elasticity and equation of state of orthoenstatite, MgSiO₃. *Am. Mineral.* **87**, 558–561 (2002).
- Ghose, S., Schomaker, V. & McMullan, R. K. Enstatite, Mg₂Si₂O₆: a neutron diffraction refinement of the crystal structure and a rigid-body analysis of the thermal vibration. *Z. Kristallogr. Cryst. Mater.* **176**, 159–175 (1986).
- Morimoto, N. & Koto, K. The crystal structure of orthoenstatite. *Z. Kristallogr. Cryst. Mater.* **129**, 65–83 (1969).
- Hawthorne, F. C. & Ito, J. Synthesis and crystal-structure refinement of transition-metal orthopyroxenes; I, Orthoenstatite and (Mg, Mn, Co) orthopyroxene. *Can. Mineral.* **15**, 321–338 (1977).
- Domeneghetti, M. C., Tazzoli, V., Ballaran, T. B. & Molin, G. M. Orthopyroxene from the Serra de Mage Meteorite; a structure-refinement procedure for a *Pbca* phase coexisting with a *C2/c* exsolved phase. *Am. Mineral.* **81**, 842–846 (1996).
- Jacob, D. et al. Ordering state in orthopyroxene as determined by precession electron diffraction. *Am. Mineral.* **98**, 1526–1534 (2013).
- Zussman, J. The crystal chemistry of pyroxenes and amphiboles. 1. Pyroxenes. *Earth Sci. Rev.* **4**, 39–67 (1968).
- Nakajima, Y., Frost, D. J. & Rubie, D. C. Ferrous iron partitioning between magnesium silicate perovskite and ferropericline and the composition of perovskite in the Earth's lower mantle. *J. Geophys. Res.* **117**, B08201 (2012).
- Kesson, S. E. & Gerald, J. Partitioning of MgO, FeO, NiO, MnO and Cr₂O₃ between magnesian silicate perovskite and magnesiowüstite: implications for the origin of inclusions in diamond and the composition of the lower mantle. *Earth Planet. Sci. Lett.* **111**, 229–240 (1991).
- Moore, R. O., Otter, M. L., Rickard, R. S., Harris, J. W. & Gurney, J. J. The occurrence of moissanite and ferro-pericline as inclusions in diamond. *Int. Kimberlite Conf. Ext. Abstr.* **4**, 406–411 (1986).
- Kaminsky, F. et al. Superdeep diamonds from the Juina area, Mato Grosso State, Brazil. *Contrib. Mineral. Petrol.* **140**, 734–753 (2001).
- Hutchison, M. T., Hursthouse, M. B. & Light, M. E. Mineral inclusions in diamonds: associations and chemical distinctions around the 670-km discontinuity. *Contrib. Mineral. Petrol.* **142**, 119–126 (2001).
- Hayman, P. C., Kopylova, M. G. & Kaminsky, F. V. Lower mantle diamonds from Rio Soriso (Juina area, Mato Grosso, Brazil). *Contrib. Mineral. Petrol.* **149**, 430–445 (2005).
- Bulanova, G. P. et al. Mineral inclusions in sublithospheric diamonds from Collier 4 kimberlite pipe, Juina, Brazil: subducted protoliths, carbonated melts and primary kimberlite magmatism. *Contrib. Mineral. Petrol.* **160**, 489–510 (2010).
- Davies, R. M., Griffin, W. L., O'Reilly, S. Y. & McCandless, T. E. Inclusions in diamonds from the K14 and K10 kimberlites, Buffalo Hills, Alberta, Canada: diamond growth in a plume? *Lithos* **77**, 99–111 (2004).
- Tappert, R., Stachel, T., Harris, J. W., Shimizu, N. & Brey, G. P. Mineral inclusions in diamonds from the Panda kimberlite, Slave Province, Canada. *Eur. J. Mineral.* **17**, 423–440 (2005).
- Davies, R. et al. Diamonds from the deep: pipe DO-27, Slave craton, Canada. *Int. Kimberlite Conf. Ext. Abstr.* **7**, 170–172 (1998).
- Tappert, R. et al. Deep mantle diamonds from South Australia: a record of Pacific subduction at the Gondwanan margin. *Geology* **37**, 43–46 (2009).
- Mendelsohn, M. J. & Milledge, H. J. Geologically significant information from routine analysis of the mid-infrared spectra of diamonds. *Int. Geol. Rev.* **37**, 95–110 (1995).
- Gu, T. & Wang, W. Optical defects in milky type IaB diamonds. *Diam. Relat. Mater.* **89**, 322–329 (2018).
- Gu, T., Ohfuji, H. & Wang, W. Origin of milky optical features in type IaB diamonds: dislocations, nano-inclusions, and polycrystalline diamond. *Am. Mineral.* **104**, 652–658 (2019).
- Gu, T., Ritterbex, S., Tsuchiya, T. & Wang, W. Novel configurations of VN₄ and VN₄H defects in diamond platelets: structure, energetics and vibrational properties. *Diam. Relat. Mater.* **108**, 107957 (2020).
- Lafuente, B., Downs, R. T., Yang, H. & Stone, N. in *Highlights in Mineralogical Crystallography* (eds Armbruster, T. & Danisi, R. M.) Ch. 1 (DeGruyter, 2015).
- Liu, L.-G., Lin, C. C., Irifune, T. & Mernagh, T. P. Raman study of phase D at various pressures and temperatures. *Geophys. Res. Lett.* **25**, 3453–3456 (1998).
- Ohtani, E., Kudoh, Y., Naito, H. & Arashi, H. Stability of dense hydrous magnesium silicate phase G in the transition zone and the lower mantle. *Mineral. J.* **20**, 163–169 (1998).
- Liu, L. G., Lin, C. C., Mernagh, T. P. & Irifune, T. Raman spectra of phase B at various pressures and temperatures. *J. Phys. Chem. Solids* **59**, 871–877 (1998).
- Cynn, H., Hofmeister, A. M., Burnley, P. C. & Navrotsky, A. Thermodynamic properties and hydrogen speciation from vibrational spectra of dense hydrous magnesium silicates. *J. Phys. Chem.* **23**, 361–376 (1996).
- Herzberg, C., Rateron, P. & Zhang, J. New experimental observations on the anhydrous solidus for peridotite KLB-1. *Geochem. Geophys. Geosyst.* **1**, 2000GC000089 (2000).
- McDonough, W. F. & Sun, S. S. The composition of the Earth. *Chem. Geol.* **120**, 223–253 (1995).
- Chanyshev, A. et al. Depressed 660-km discontinuity caused by akimotoite–bridgmanite transition. *Nature* **601**, 69–73 (2022).
- Yu, Y. G., Wentzcovitch, R. M., Vinograd, V. L. & Angel, R. J. Thermodynamic properties of MgSiO₃ majorite and phase transitions near 660 km depth in MgSiO₃ and Mg₂SiO₄: a first principles study. *J. Geophys. Res.* **116**, 31–19 (2011).

76. Nishiyama, N., Irifune, T., Inoue, T., Ando, J.-I. & Funakoshi, K.-I. Precise determination of phase relations in pyrolyte across the 660 km seismic discontinuity by in situ X-ray diffraction and quench experiments. *Phys. Earth Planet. Inter.* **143–144**, 185–199 (2004).
77. Wood, B. J. & Rubie, D. C. The effect of alumina on phase transformations at the 660-kilometer discontinuity from Fe–Mg partitioning experiments. *Science* **273**, 1522–1524 (1996).

Acknowledgements

This research was supported by a GIA Liddicoat Postdoctoral Research Fellowship to T.G. Sincere thanks to T. Moses from GIA for access to this sample; J. W. Valley and B. L. Dutrow for their support on GIA research program; E. Yazawa and C. Zhou from GIA for technical assistance; K. Moe from GIA for assistance with Raman data collection; J. I. Koivula, N. D. Renfro and J. Liao from GIA for photomicrography; U. D’Haenens-Johansson from GIA for sample selection; E. Smith, K. Smit and M. Y. Krebs from GIA for valuable discussion; R. Passeri, Jr from Hitachi and A. Chan from GIA for assisting in sample preparation; and S. D. Jacobsen from NU for discussions and providing supplementary Raman data. M.G.P. has received funding from the European Union’s Horizon 2020 Marie Skłodowska-Curie grant agreement no. 796755. D.N. acknowledges the ‘Rita Levi Montalcini’ programme of the Italian Ministry of University and Research. M.A. is supported by a European Research Council (ERC) grant agreement no. 714936 TRUE DEPTHS. F.N. thanks the ERC Starting Grant no. 307322 and the Alexander von Humboldt Foundation. Sincere thanks to O. Navon for constructive comments.

Author contributions

T.G. prepared optical images, polished the diamond, performed and interpreted micro-Raman, FTIR and EMPA. F.N. and T.G. performed and interpreted X-ray diffraction. J.F. assisted sample preparation and performed EMPA. T.G. and F.N. wrote the initial draft of the manuscript. T.G., M.G.P., D.N. and F.N. interpreted and wrote mineral physics and petrological parts. M.A. and F.E.B. helped in writing the manuscript. F.E.B. also helped with sample preparation for microprobe analyses. W.W. helped guide the project and ensured access to analytical resources.

competing interests

The authors declare no competing interests.

Additional information

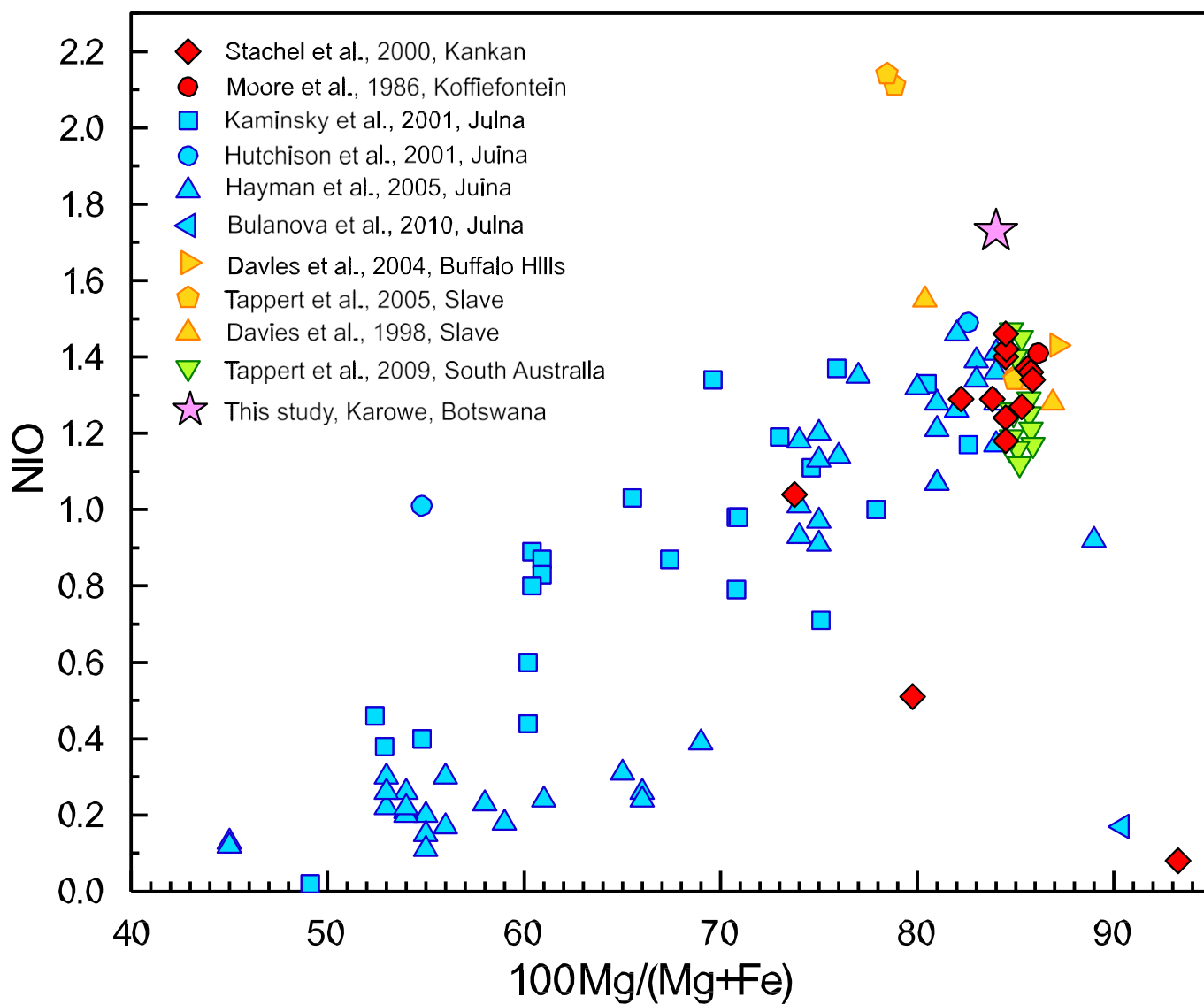
Extended data is available for this paper at <https://doi.org/10.1038/s41561-022-01024-y>.

Supplementary information The online version contains supplementary material available at <https://doi.org/10.1038/s41561-022-01024-y>.

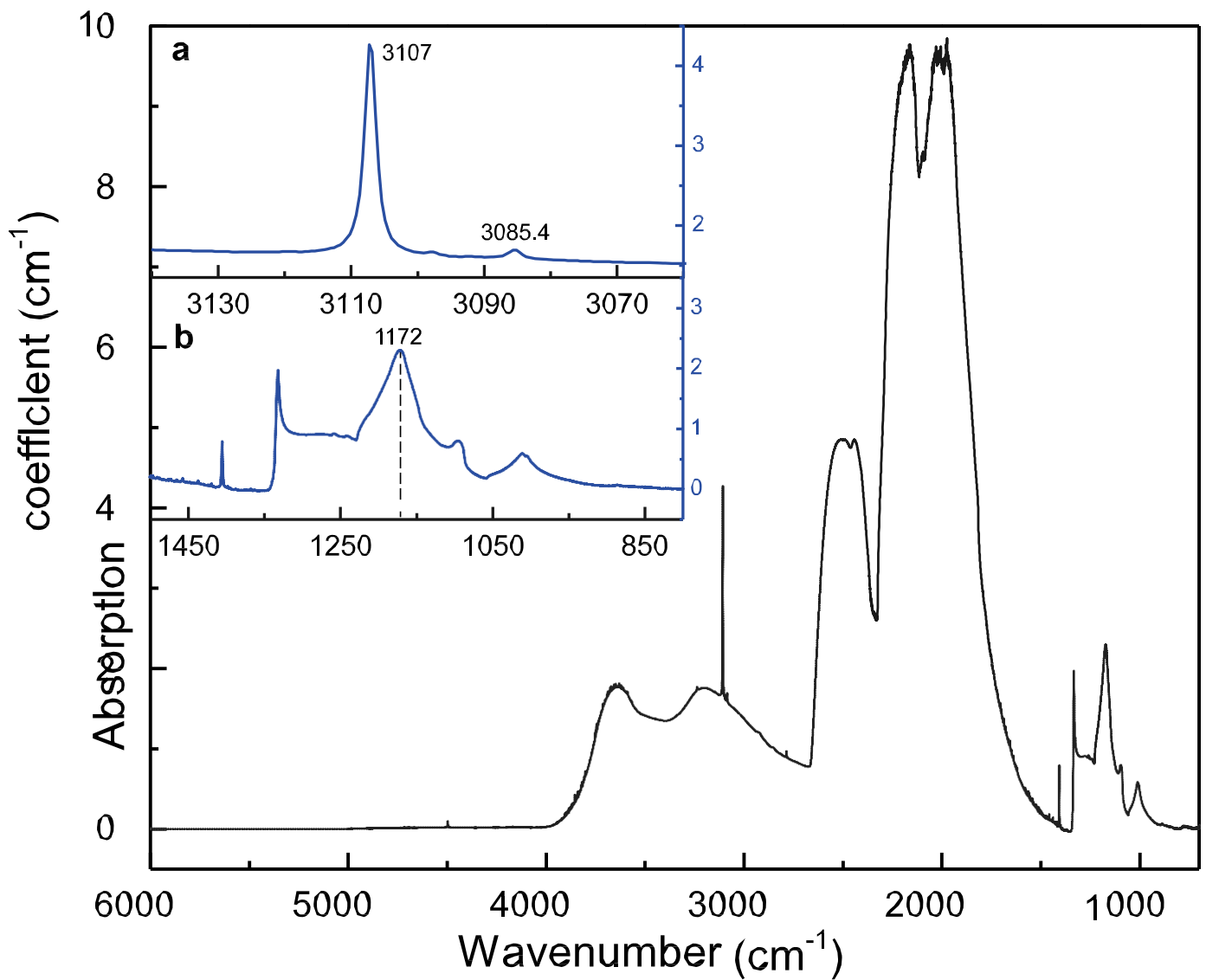
Correspondence and requests for materials should be addressed to Tingting Gu or Fabrizio Nestola.

Peer review information *Nature Geoscience* thanks Qingyang Hu and the other, anonymous, reviewer(s) for their contribution to the peer review of this work. Primary Handling Editor: Rebecca Neely, in collaboration with the *Nature Geoscience* team.

Reprints and permissions information is available at www.nature.com/reprints.



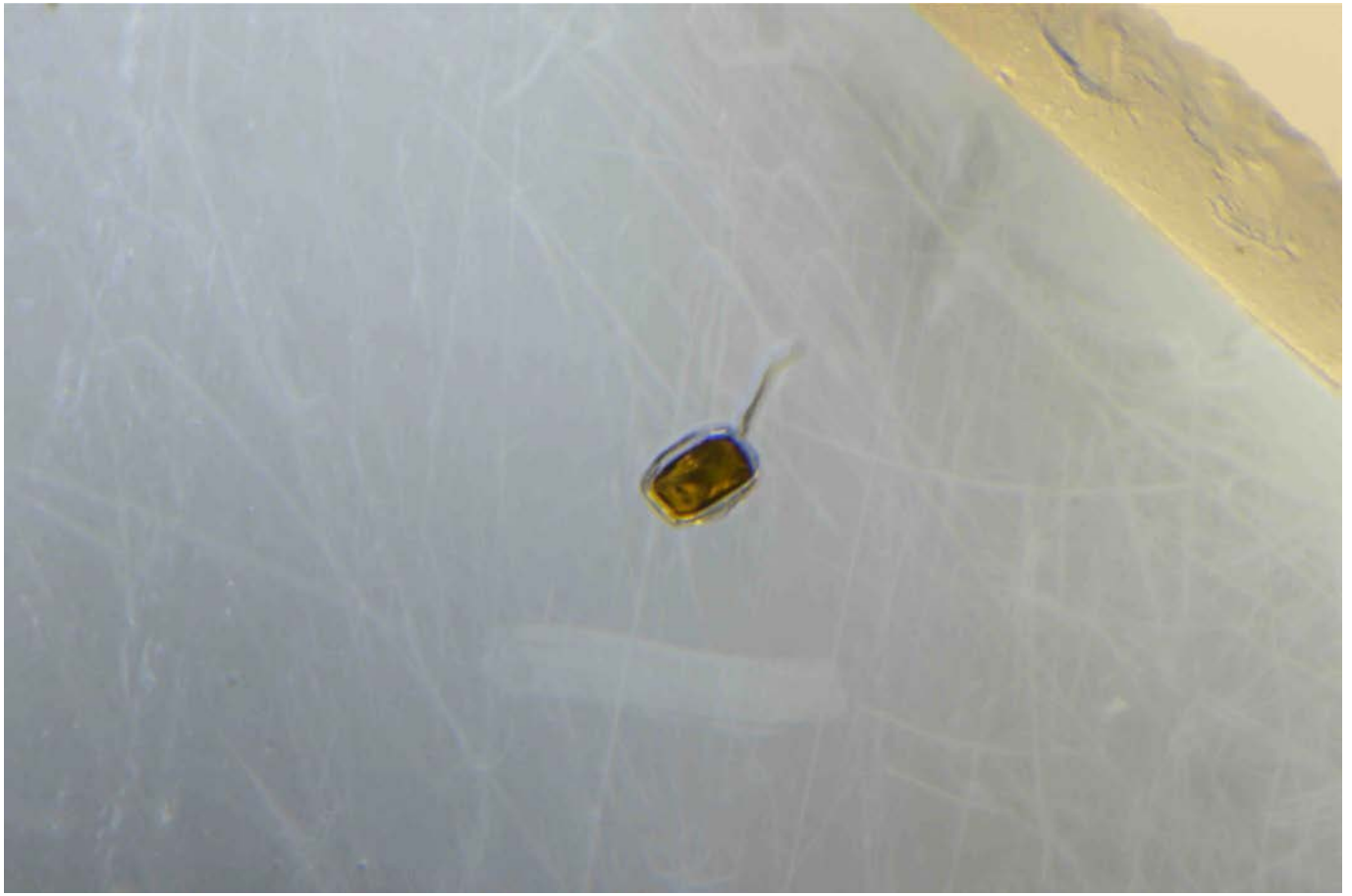
Extended Data Fig. 1 | NiO content of ferropericlase in worldwide super deep diamonds. NiO content (wt%) versus molar Mg number for ferropericlase inclusions in diamonds from this study (Karowe, Botswana) and world-wide sources of super deep diamonds from Kankan²⁶, Koffiefontein⁵⁴, Juina^{55–58}, Buffalo hills⁵⁹, Slave^{60,61}, and South Australia⁶².



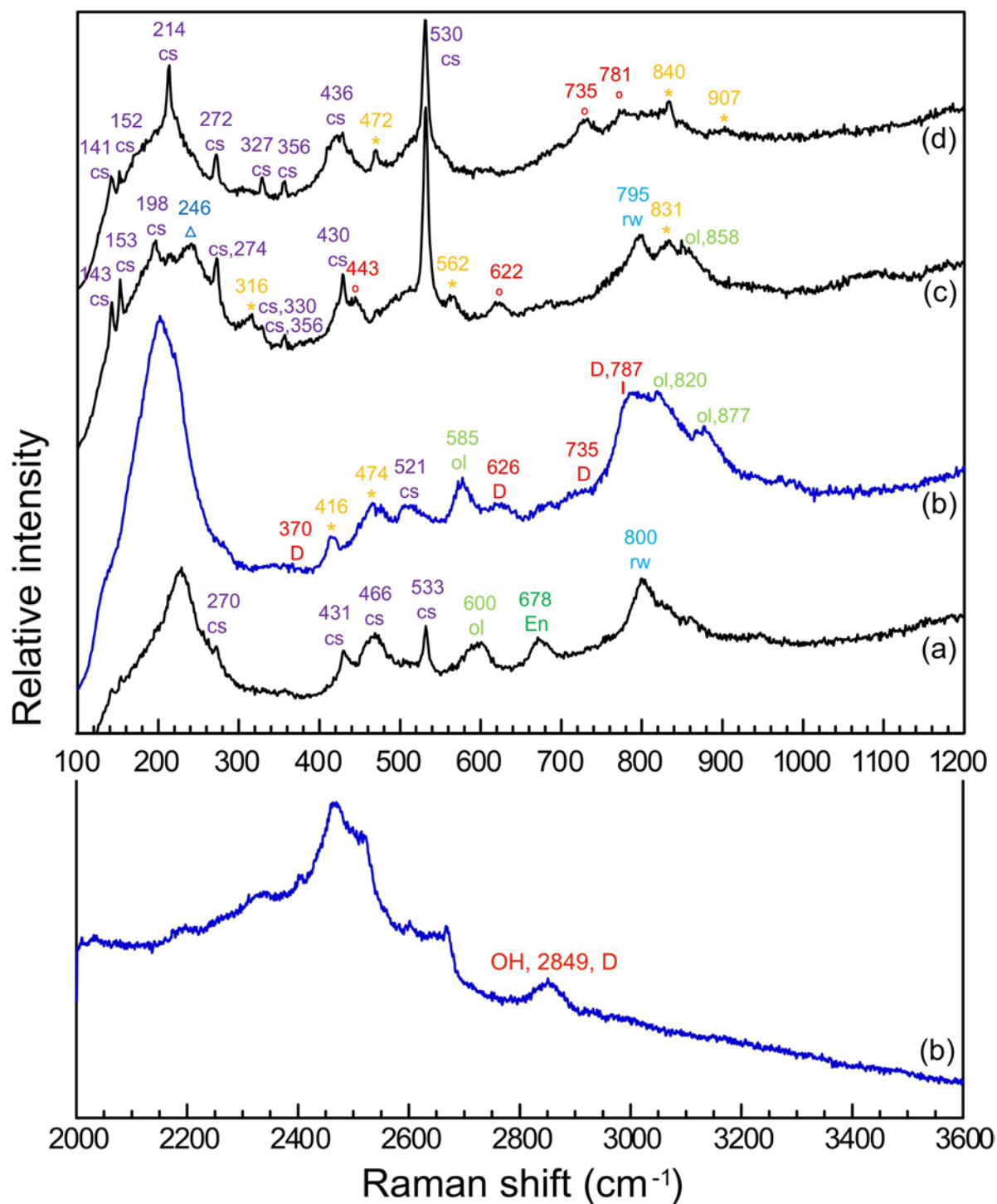
Extended Data Fig. 2 | FTIR spectra of the 1.5 ct diamond. The spectrum was baselined in GRAMS software and normalized by two-phonon diamond lattice bands at 2460 cm⁻¹⁶³, showing that it is a pure type IaB diamond with only B center nitrogen. Inset figure (a) shows hydrogen related peaks at 3107 and 3085 cm⁻¹, which are typical in milky type IaB diamonds^{64,65} and consistent with the milky feature observed around inclusion 3. Inset figure (b) shows B center nitrogen at 1172 cm⁻¹ with no detectable A center nitrogen and very weak residual IR absorption at 1367 cm⁻¹ caused by hydrogen related defects incorporated into platelets that quench the platelet IR absorption⁶⁶. Source data



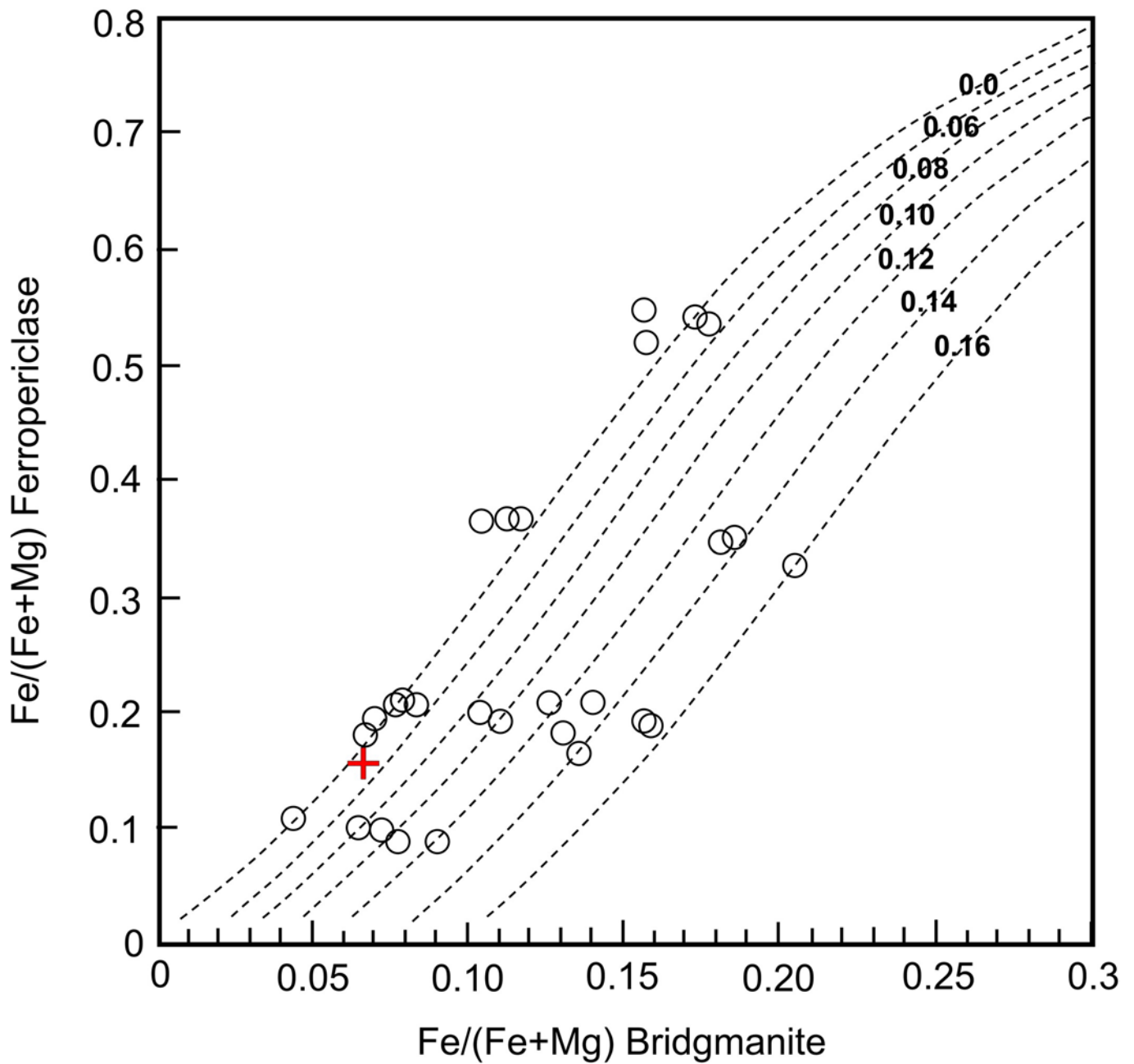
Extended Data Fig. 3 | optical images of other inclusions found in the 1.5 ct diamond. Inclusion 3 is a cluster of submicron sized inclusions (inc3a), surrounded by pin points that generate a milky appearance (inc3b), which could be octahedral or elongated nano sized inclusions filled with nitrogen rich fluids⁶⁵. Inclusion 7 and 12 did not show any detectable Raman bands. Inclusion 9 is opaque in the center and close to the mineral assemblage of inclusion 2. Its appearance and Raman spectra (Extended databases) imply that it is likely a ferropericlase phase as the by-product from the decomposed ringwoodite. Inclusion 13 is a polyphasic assemblage without diagnostic Raman spectra, while the individual minerals are too small to be precisely probed by XRD (the shortest dimension is less than 10 μm). Field views of each image from inc3a to inc13 are 2.87, 1.40, 1.60, 0.91, 0.91, 0.96 mm.



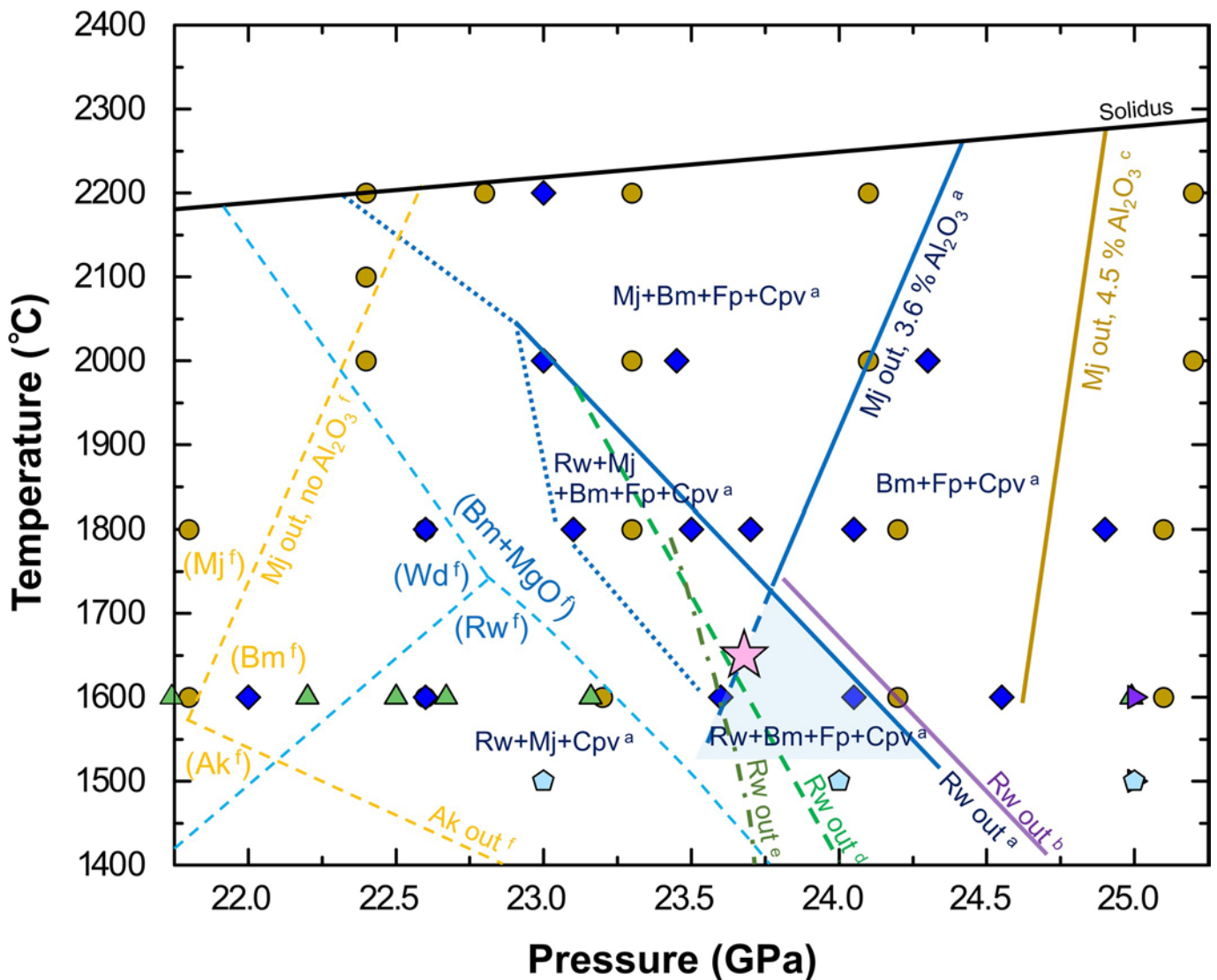
Extended Data Fig. 4 | optical image of inclusion 11. Scratches on the surface are marks in the Ir coating, after EMPA. Field view is 0.91 mm.



Extended Data Fig. 5 | raman spectra for inclusion 2c at different areas (a-d). Coesite (cs) peaks (RRUFF ID: X050094⁶⁷) have been observed in almost all spectra; the peaks in area (a) and (c) at ~ 800 and 858 cm^{-1} are assigned to ringwoodite (rw) or partially retrogressed olivine (ol), possibly accompanied by enstatite (En) in (a). Diagnostic Raman peaks have been observed in (b) at ~ 787 , 735 , 626 , 375 cm^{-1} , which could be assigned to phase D (D). The accompanied vibration at ~ 2849 cm^{-1} in (b) is consistent with the OH stretching of phase D^{23,68,69}. A few peaks at ~ 781 and 735 cm^{-1} seem recurring in (d). Spectra were collected at GIA. Red circle, triangle, orange stars: undefined peaks. The orange stars with the peak around 831 cm^{-1} could be overlapped with other hydrous phase such as super hydrous phase B^{70,71}.



Extended Data Fig. 6 | Fe partition between bridgmanite and ferropericlasite. Fe partition between bridgmanite and ferropericlasite at different amounts of Al content in bridgmanite in atoms per formula unit adopted from previous study at 24 GPa, 1650 °C²⁹. Red cross marks the data observed in this study based on the molar Fe/(Fe+Mg) ratio of bridgmanite and ferropericlasite, which falls into the range of Al ~0.024 per formula unit.



Extended Data Fig. 7 | Phase relations in the pyrolitic mantle composition. Solidus curve is from⁷². ^a Solid blue diamonds and lines are from pyrolitic mantle composition KLB-1 with slightly depleted bulk $\text{Al}_2\text{O}_3 \sim 3.6$ wt.%²⁴. Coexisting mineral assemblages have been marked by dark blue text. Note that the transition of ringwoodite (Rw) to bridgmanite (Bm), ferropericlase (Fp) and Ca-perovskite (Cpv) has a negative Clapeyron slope (Rw out line), while the transition of majorite garnet (Mj) to bridgmanite and ferropericlase has a positive Clapeyron slope (Mj out line). ^b Solid blue pentagons are from pyrolitic mantle composition and the solid purple line is the estimated line for ringwoodite phase transition which is between 24 to 25 GPa at 1500 °C³¹. ^c Solid brown circles and lines³³ are from pyrolitic mantle composition⁷³ with ~ 4.5 wt.% bulk Al_2O_3 content. The phase transition pressure of majorite garnet to bridgmanite and ferropericlase is slightly higher than that with lower Al content in the bulk sample²⁴. ^d Dashed green line represents the transition of ringwoodite (Mg_2SiO_4) to bridgmanite and periclase constrained by a precise internal MgO pressure scale³⁰. ^e Dashed dark green line is from the most recent data of the phase boundary of ringwoodite (Mg_2SiO_4) bridgmanite and periclase constrained by in situ X-ray diffraction in a multi-anvil press⁷⁴. ^f Phase relations of ringwoodite, wadsleyite (Wd), bridgmanite and periclase in a Mg_2SiO_4 system (dashed light blue lines) as well as akimotoite (Ak), majorite garnet, bridgmanite in a MgSiO_3 system (dashed orange lines) calculated by density functional theory are plotted for comparison^{24,75}. Results from previous studies on the pyrolitic mantle composition with green⁷⁶ and purple triangles⁷⁷ are also plotted. *Note that the dashed lines represent data constrained in a Mg-Si-O system (without Fe or Al). The pink star is the reference spot indicating the phases expected in a pyrolitic mantle composition that falls in the range of our calculated temperature and the corresponding pressure at the phase equilibrium.